

High-sensitivity THz evanescent field sensing of biomolecules using on-chip systems

Binbin Hong¹, Kun Meng², Yanbing Qiu³, Zhaohui Zeng⁴,
Ian Robertson⁵, John Cunningham⁵, and Nutapong Somjit⁵

¹ Faculty of Arts and Sciences, Beijing Normal University, Zhuhai 519085, China.

² Qingdao QUENDA Terahertz Technology Co. Ltd, Qingdao 266104, China

³ Institute of Microscale Optoelectronics, Shenzhen University, Shenzhen 518060, China.

⁴ Institute of Semiconductors, Guangdong Academy of Sciences, Guangzhou 510650,
China

⁵ School of Electronic and Electrical Engineering, University of Leeds, Leeds LS2 9JT,
UK

Authors to whom correspondence should be addressed: [Binbin Hong,

b.hong@bnu.edu.cn; Nutapong Somjit, n.somjit@leeds.ac.uk]

Abstract: We present a THz sensing chip capable of detecting trace biomolecules. Its operating bandwidth stretches from 0.2 to 1.35 THz, capable of signal strengths exceeding 38 dB above noise levels, achieved by the mitigation of mode competition issues. The high sensitivity of the sensing chip is used to observe the absorption fingerprints of α -lactose monohydrate, L-tyrosine, and L-histidine powders at their characteristic frequencies for sample masses as low as 0.3 mg. Using a solution titration technique, we demonstrate detection of the absorption fingerprint of α -lactose monohydrate for concentrations of 72 $\mu\text{g}/\mu\text{L}$, adding just 57.6 μg of the powder onto the chip after evaporation of the ethanol solvent, representing a two-fold advancement over prior work by providing a significantly broader operating spectrum and higher sensitivity. The relatively easy manufacturability, low cost, and scalability of the sensing chip paves the way for studies of enhanced light-matter interaction between THz waves and trace analytes, while also unlocking innovative potential applications in biomolecular sensing, medical diagnostics, and environmental monitoring.

Terahertz (THz) waves (0.1–10 THz) exhibit properties in time, space, and photon energy, linked to phenomena in the microscopic world, offering substantial scientific research opportunities [1-2]. The THz frequency range covers spectral regions of phonons, magnons, low-energy excitations, and molecular vibrations [3]. It encompasses fundamental processes such as rotational and vibrational transitions in molecules, lattice vibrations, intra-band transitions in semiconductors, and superconductor band transitions [3, 4]. Sub-picosecond THz pulses analyze ultra-fast molecular dynamics, like vibrational and rotational motions. Molecular vibrational dynamics on sub-picosecond timescales are critical to chemical function and structure [5-8]. Studies of short-range atomic and molecular interactions have been extensive within the infrared range [9, 10]. Currently, the study of long-range and intermolecular vibrational modes occurring on sub-picosecond timescales (corresponding to THz frequencies) and related to molecular conformation [11], reaction dynamics [12], and biological functions [5] is an emerging and active frontier in research. Numerous emerging materials, such as biomacromolecules [13], two-dimensional materials [14], and quantum thin films [15], have characteristic sizes at the nanoscale, considerably smaller than the wavelength of THz waves. The small scattering cross-section between THz waves and materials limits their interaction with free-space THz waves. Therefore, detecting their unique spectral signatures using conventional free-space THz spectroscopy is challenging. Alternatively, waveguide systems are developed to enhance THz light-matter interactions, offering tight field confinement and extended interaction lengths.

Advances in THz waveguides enhance light-matter interactions by confining fields to sub-wavelength regions, surpassing the diffraction limit. [16, 17]. Metallic transmission lines like microstrip offer broad single-mode bandwidth for on-chip THz sensing, while the evanescent field enables direct interaction with nearby materials. Such on-chip systems offer bandwidths over 1.2 THz, detecting lactose molecules with absorption fingerprints like those in free space. [18]. Additionally, modified versions of this on-chip system have been used to

qualitatively detect organic solvents such as methanol, ethanol, and propanol [19], to effectively differentiate solutions of varying concentrations of isopropanol [20], and to measure the hybridization state of overlaid DNA films [21, 22]. Kadoya *et. al.* exploited the geometry of coplanar strip-lines and used on-chip systems for fingerprint spectrum identification of biotin powder [23]. Notably, besides lactose, biotin powder, as well as more conventional targets like oil and alcohol compounds were studied. THz on-chip enhanced sensing can also detect a wider range of target materials. For example, Kitagawa *et. al.* used an on-chip system to capture the THz phonon modes of n-Ba₈Ga₁₆Ge₃₀ [24]. Toshihiko *et. al.* utilized on-chip systems for label-free DNA hybridization sensing by exploiting the different THz time-domain signal delay characteristics of various DNA conformations [25]. Cunningham *et. al.* also used on-chip systems to study THz frequency magneto-plasmonic resonances in two-dimensional electron systems [26], providing insights into the study of ultrafast carrier dynamics in low-dimensional semiconductor nanostructures within the THz frequency range.

In our previous work [27], we demonstrated the efficient coupling of ultrafast sub-picosecond THz pulses from free-space to a chip utilizing an ultra-wideband Vivaldi antenna and a slotline waveguide. In this paper, we investigate and experimentally demonstrate a THz sensing chip designed for broadband and highly sensitive fingerprint detection of trace substances, surpassing the diffraction limit. The improved chip resolves mode competition, expanding the bandwidth to 0.2-1.35 THz. The design features a THz wave tightly confined and significantly enhanced around the central gap of a 25- μm -wide slotline waveguide, significantly smaller than typical THz wavelengths ($\sim 300 \mu\text{m}$). The proposed THz sensing chip offers fast production, low cost, and scalability, making it a promising platform for THz light-matter interactions.

The THz sensing chip features back-to-back Vivaldi antennas with a 90° bent slotline waveguide in between, as shown in Figure 1(a)-(c). During measurements, the material-under-test (MUT) is placed above the central region of the waveguide where the electric field strength

is significantly increased near the 25 μm gap, enhancing interaction with the MUT. The inner edge of the slotline waveguide is extended with a circular section to mitigate the influence of competing edge modes on the primary THz signal pulse, as detailed in Section 3.

A 13 μm thick polyimide thin film was used as the substrate to inhibit TM mode transmission, which has a high-pass characteristic; thinner substrates increase the cutoff frequency, reducing the mode competition with the fundamental mode (FM). Two ultra-wideband Vivaldi antennas, each $w=0.62$ mm and $l=1.6$ mm, enhanced the coupling of terahertz waves between free space and the chip. A 90° bent slotline waveguide with a 25 μm gap was positioned between the antennas, optimizing THz wave confinement and bandwidth transmission. The antennas and waveguide were fabricated using ultraviolet mask exposure, and electron beam evaporation, with a multilayer metal thin film of Ti/Ag/Ti (10/300/10 nm). Silver was chosen for its high electrical conductivity, improving transmission efficiency over gold (see Figure S1 in the supplementary material). Detailed micro-nano fabrication processes and batch production information are available in Figures S2 and S3.

Figure 1(d) shows the measurement setup for the sensing chip, using a THz-TDS system equipped with a 1560 nm femtosecond fiber laser (TERA K15, MenloSystems Corp.) and TPX lenses to focus THz radiation into the slotline waveguide. The system includes fiber-coupled THz emitter and receiver with an InP-based InGaAs/InAlAs structure to emit and detect THz signals, housed in a nitrogen-filled acrylic box to minimize water vapor absorption, with the chip mounted on low-loss EPS foam. Further details on EPS foam's THz dielectric properties are in Figure S4.

To evaluate the confinement of the slotline waveguide and the efficiency of antenna coupling, Figure 2 displays the propagation properties from CST FDTD simulations. The substrate (Polyimide) and metal (Ag) were modeled as lossy materials from the CST material library, with "open" boundary conditions applied at the outer edges of the simulation area. Figure 2(a) displays the simulated electric field intensity at frequencies of 0.2, 0.5, 0.8, and 1.1

THz, demonstrating effective wave confinement and strong electromagnetic interaction. Figure 2(b) shows the transmission remains above -3.90 dB across 0.2-2.8 THz, peaking at -1.36 dB at 1.17 THz, while reflection stays below -20 dB from 0.5-2.8 THz, indicating efficient waveguide performance with low reflection loss over a wide bandwidth.

Figures 2(c)-(f) present the near-field and far-field simulation results for the Vivaldi antenna. Simulations show efficient transition from waveguide to free space over a wide bandwidth (Figures 2(c)-(d)), with reflection below -10 dB in the 0.3-2.8 THz range, indicating good impedance matching and strong signal coupling onto the chip. Figures 2(e) present the far-field radiation pattern at several representative frequency points. For lower frequencies, (0.2 THz to 0.5 THz), the Vivaldi antenna exhibits good directivity with a single main lobe, though by 0.8 THz, the radiation pattern begins to show multi-directionality; at 1.1 THz more pronounced side lobes appear. This results in less efficient radiation patterns and reduced directivity at higher frequencies. Figure 2(f) illustrates the coupling efficiency of the Vivaldi antenna, calculated based on the method outlined in our previous work [27]. Briefly, the total insertion loss of the sensing chip was first obtained by comparing the measured on-chip and free-space amplitudes (see Figure 4(b)). Then, the slotline waveguide's insertion loss, determined through CST simulations (see Figure 2(b)), was subtracted to isolate the insertion loss of the Vivaldi antenna. From this, the coupling efficiency was derived. As shown in Figure 2(f), the coupling efficiency exceeds 50% near 0.5 THz, reaching a peak of 52.6% at 0.45 THz. Beyond this point, the efficiency decreases at both lower and higher frequencies, reflecting the dimensional characteristics of the Vivaldi antenna.

During chip testing, an oscillatory peak was noted before the main terahertz signal (Figure 3(f), black curve), adversely affecting the frequency spectrum after Fast Fourier Transform (FFT) by introducing spurious absorption peaks and reducing smoothness. This phenomenon is counterproductive to our goal of achieving broadband fingerprint spectroscopy. Therefore, it is imperative to identify the cause of this oscillatory peak and mitigate its

influence.

To address this issue, we conducted numerical simulations analyzing the propagation modes of the THz sensing chip. First, the eigenmodes in the slotline waveguide were analyzed using the Eigenmode Solver in CST Studio. Figure 3(a) shows part of the slotline waveguide and the entire Vivaldi antenna. A segment of the slotline waveguide was used as a unit cell in CST to calculate its eigenmodes, as depicted in Figure 3(b). Here, point A corresponds to the outer circular edge of the sensing chip, point B to the channel of the slotline waveguide, and point C to the inner circular edge of the chip. Figures 3(c), (d), and (e) present the electric field modes at points A, B, and C on the unit cell, respectively.

It is evident that the mode shown in Figure 3(d) at point B is the desired FM. However, the sensing chip exhibits several competing modes. Notably, we observe two modes (Competing Mode 1 (CM1) at the outer round edge (Figure 3c) and Competing Mode 2 (CM2) at the inner round edge (Figure 3e)) that significantly influence the results. Experiments discussed in the supplementary note 5 indicate that it is CM2 that causes oscillations before the primary THz signal pulse, owing to its shorter transmission distance compared to the FM. Conversely, CM1 is observed to have a negligible effect on test results, likely due to higher radiation loss at the outer bend of the chip.

To mitigate the effects of CM2, we extended an extra circular section at the inner edge of the chip, increasing the transmission distance of the competing mode and thereby minimizing its impact on FFT analysis by placing its oscillation outside the critical time window. This adjustment also enhances the reflection and radiation loss of CM2. Figure 3(f) shows the time-domain spectrum with and without the modification, highlighting the reduced oscillation impact of the extended section, validating the effectiveness of the adjustment in suppressing unwanted signals. Further shape variations beyond the circular extension at the inner chip edge have been explored, detailed in Supplementary Figures S5-S7, with the circular design proving most efficient.

Figure 4(a) displays the THz time-domain signal with and without the unloaded sensing chip, as set up in Figure 1(d), including an inset of the chip on EPS foam. A 40 ps time window was used to avoid Fabry-Perot effects, yielding a frequency resolution of 7.35 GHz. Figure 4(b) shows the THz amplitude spectrum, covering an effective range of 0.2 to 1.35 THz with a dynamic range exceeding 38 dB, peaking at 73 dB at 0.45 THz, but dips near 1.4 THz due to resonances, thus setting the operational band just below this point. Figures 4(c) and (d) compare time-domain signals and frequency spectra across chips, confirming consistent shape, magnitude, and minimal spectral variation, thereby validating measurement reproducibility and reliability.

We validated the fingerprint sensing capabilities of the sensor chip by testing three biomolecules: α -lactose monohydrate, L-histidine, and L-tyrosine. Initially, terahertz spectra of these powders were acquired in free space to identify absorption peak frequencies, followed by on-chip sensing tests. The correspondence of absorption peaks between the chip and free space confirmed the chip's efficacy. In terms of the method of applying the powder, an appropriate amount was first placed on the slotline waveguide using a spoon. This was followed by gently compacting the powder with the spoon to ensure improved adherence to the transmission channel. An electronic balance measured the weight of the chip before and after adding the powder to determine the powder's mass.

Figure 5 shows the THz signals and their corresponding spectra for the three types of powders, both obtained in free space and using the sensing chip. The black curve represents data acquired in free space, while the colored curve is obtained using the sensing chip. Figures 5(a)-(c) show the THz signals of α -lactose monohydrate, L-histidine, and L-tyrosine, respectively. The on-chip THz pulse strength is about one-sixth of the free-space pulse. This decrease in amplitude is attributed to a combination of antenna coupling loss, slotline waveguide transmission loss, and scattering and absorption losses from the sample. Figures 5(d)-(f) present their frequency spectra calculated after Fast Fourier Transform (FFT).

Specifically, Figure 5(a) illustrates the spectrum of α -lactose monohydrate powder measured both in free space and with the chip, highlighting that the main peak in the frequency spectrum occurs at approximately 0.525 THz in both scenarios. Additionally, Figures 5(e) and (f) show that the spectral absorption peaks of L-histidine and L-tyrosine, obtained in free space and with the chip, appear at 0.774 THz and 0.974 THz, respectively. This indicates that the sensing chip is effective in detecting these three types of powders and identifying their characteristic absorption peaks. Table 1 accompanying the Figure lists the positions of the main absorption peaks in the spectra of these three powders, both in free space and as obtained by the sensing chip, along with the mass used for each measurement.

Solution titration was employed to reduce the quantity of powder added to the chip. Specifically, powders of varying masses were mixed with anhydrous ethanol to form solutions of different concentrations. Equal volumes of these solutions at varying concentrations were extracted using a micropipette and applied at the center of the transmission channel of the chip. The ethanol rapidly evaporated, leaving only the powder to be measured on the sensor chip. α -lactose monohydrate-ethanol suspensions were prepared with 72, 108, and 144 $\mu\text{g}/\mu\text{L}$ concentrations. Figure 6 shows the spectrum of the sensor chip with the addition of 0.8 μL of anhydrous ethanol and suspensions at different concentrations. As evident from the Figure, the spectrum for the sensor chip with added α -lactose monohydrate displays a distinct absorption peak at 0.525 THz. Furthermore, as the quantity of α -lactose monohydrate powder on the sensor chip increases, the characteristic absorption peak of α -lactose monohydrate in the spectrum becomes more pronounced. We note that the spectrum obtained from the sensing chip with the addition of only anhydrous ethanol is smooth, showing no absorption peaks, indicating that ethanol does not affect the terahertz signal on the chip. The experimental data indicates that the THz sensing chip can effectively detect α -lactose monohydrate in ethanol at concentrations as low as 72 $\mu\text{g}/\mu\text{L}$, requiring only the deposition of 57.6 μg of α -lactose monohydrate on the chip, followed by solvent evaporation.

Table 2 compares broadband THz spectroscopy studies on α -lactose monohydrate, including free-space and on-chip THz-TDS methods. The proposed THz sensing chip shows a two-order-of-magnitude improvement in sensitivity, reducing the required lactose concentration for detection compared to other studies.

In summary, we have developed a broadband, highly sensitive THz sensing chip featuring Vivaldi antennas and a slotline waveguide. The antennas efficiently couple THz waves to and from free space optics, offering broad bandwidth and strong signal intensity. The slotline waveguide effectively confines electromagnetic waves, enhancing material interactions. An extended circular section at the waveguide's inner edge suppresses competing transmission modes, stabilizing the signal and improving test reliability. Without load, the chip operates between 0.2 and 1.35 THz, achieving a dynamic range up to 73.57 dB. Our experiments confirm the chip's stability and repeatability, detecting characteristic spectra of α -lactose monohydrate, L-tyrosine, and L-histidine within its bandwidth. We applied 57.6 μg of α -lactose monohydrate using solution titration, detecting its distinct absorption features at a remarkably low concentration of 72 $\mu\text{g}/\mu\text{L}$. This technology promises significant advances in trace-sensing applications.

See supplementary material for supporting content of this paper.

This work was supported in part by the National Natural Science Foundation of China (Grant Nos. 62105213), and by the Beijing Natural Science Foundation (Grant No. Z240008), and EPSRC grant EP/V047914/1.

AUTHOR DECLARATIONS

Conflict of Interest

The authors have no conflicts to disclose.

Author Contributions

Binbin Hong and **Kun Meng** conceived the idea and supervised the whole project; **Binbin Hong** and **Yanbing Qiu** carried out the theoretical analysis, **Yanbing Qiu** performed the numerical simulations and experimental data processing; **Yanbing Qiu** and **Zhaohui Zeng** performed the fabrications and measurements; **Ian Robertson**, **John Cunningham** and **Nutapong Somjit** participated in the analysis and the discussion of the results; **Binbin Hong** wrote the manuscript with input from all other authors.

DATA AVAILABILITY

The data that support the findings of this study are available from the corresponding author upon reasonable request.

REFERENCES

1. Dhillon, S.S., Vitiello, M.S., Linfield, E.H., Davies, A.G., Hoffmann, M.C., Booske, J., Paoloni, C., Gensch, M., Weightman, P., Williams, G.P. and Castro-Camus, E., 2017. The 2017 terahertz science and technology roadmap. *Journal of Physics D: Applied Physics*, 50(4), pp.043001.
2. Leitenstorfer, A., Moskalenko, A.S., Kampfrath, T., Kono, J., Castro-Camus, E., Peng, K., Qureshi, N., Turchinovich, D., Tanaka, K., Markelz, A.G. and Havenith, M., 2023. The 2023 terahertz science and technology roadmap. *Journal of Physics D: Applied Physics*, 56(22), pp.223001.
3. Ho, L., Pepper, M. and Taday, P., 2008. Signatures and fingerprints. *Nature Photonics*, 2(9), pp.541-543.
4. Davies, A.G., Burnett, A.D., Fan, W., Linfield, E.H. and Cunningham, J.E., 2008. Terahertz spectroscopy of explosives and drugs. *Materials Today*, 11(3), pp.18-26.

5. Markelz, A.G., 2008. Terahertz dielectric sensitivity to biomolecular structure and function. *IEEE Journal of Selected Topics in Quantum Electronics*, 14(1), pp.180-190.
6. Zhang, L., Wang, L., Kao, Y.T., Qiu, W., Yang, Y., Okobiah, O. and Zhong, D., 2007. Mapping hydration dynamics around a protein surface. *Proceedings of the National Academy of Sciences*, 104(47), pp.18461-18466.
7. Taday, P.F., 2004. Applications of terahertz spectroscopy to pharmaceutical sciences. *Philosophical Transactions of the Royal Society of London. Series A: Mathematical, Physical and Engineering Sciences*, 362(1815), pp.351-364.
8. Fischer, B., Hoffmann, M., Helm, H., Modjesch, G. and Jepsen, P.U., 2005. Chemical recognition in terahertz time-domain spectroscopy and imaging. *Semiconductor Science and Technology*, 20(7), pp.S246.
9. Movasaghi, Z., Rehman, S. and Rehman, I.U., 2007. Raman spectroscopy of biological tissues. *Applied Spectroscopy Reviews*, 42(5), pp.493-541.
10. Movasaghi, Z., Rehman, S. and ur Rehman, D.I., 2008. Fourier transform infrared (FTIR) spectroscopy of biological tissues. *Applied Spectroscopy Reviews*, 43(2), pp.134-179.
11. Walther, M., Plochocka, P., Fischer, B., Helm, H. and Uhd Jepsen, P., 2002. Collective vibrational modes in biological molecules investigated by terahertz time-domain spectroscopy. *Biopolymers: Original Research on Biomolecules*, 67(4-5), pp.310-313.
12. Hay, S. and Scrutton, N.S., 2012. Good vibrations in enzyme-catalysed reactions. *Nature Chemistry*, 4(3), pp.161-168.
13. Sun, L., Zhao, L. and Peng, R.Y., 2021. Research progress in the effects of terahertz waves on biomacromolecules. *Military Medical Research*, 8, pp.1-8.
14. Gopalan, P. and Sensale-Rodriguez, B., 2020. 2D materials for terahertz modulation. *Advanced Optical Materials*, 8(3), pp.1900550.
15. Yang, C.J., Li, J., Fiebig, M. and Pal, S., 2023. Terahertz control of many-body dynamics in quantum materials. *Nature Reviews Materials*, 8(8), pp.518-532.

16. McIver, J.W., Schulte, B., Stein, F.U., Matsuyama, T., Jotzu, G., Meier, G. and Cavalleri, A., 2020. Light-induced anomalous Hall effect in graphene. *Nature Physics*, 16(1), pp.38-41.
17. Gallagher, P., Yang, C.S., Lyu, T., Tian, F., Kou, R., Zhang, H., Watanabe, K., Taniguchi, T. and Wang, F., 2019. Quantum-critical conductivity of the Dirac fluid in graphene. *Science*, 364(6436), pp.158-162.
18. Byrne, M.B., Cunningham, J., Tych, K., Burnett, A.D., Stringer, M.R., Wood, C.D., Dazhang, L., Lachab, M., Linfield, E.H. and Davies, A.G., 2008. Terahertz vibrational absorption spectroscopy using microstrip-line waveguides. *Applied Physics Letters*, 93(18), pp.182904.
19. Russell, C., Swithenbank, M., Wood, C.D., Burnett, A.D., Li, L., Linfield, E.H., Davies, A.G. and Cunningham, J.E., 2016. Integrated on-chip THz sensors for fluidic systems fabricated using flexible polyimide films. *IEEE Transactions on Terahertz Science and Technology*, 6(4), pp.619-624.
20. Swithenbank, M., Burnett, A.D., Russell, C., Li, L.H., Davies, A.G., Linfield, E.H., Cunningham, J.E. and Wood, C.D., 2017. On-chip terahertz-frequency measurements of liquids. *Analytical chemistry*, 89(15), pp.7981-7987.
21. Tiang, C.K., Cunningham, J., Wood, C., Hunter, I.C. and Davies, A.G., 2006. Electromagnetic simulation of terahertz frequency range filters for genetic sensing. *Journal of Applied Physics*, 100(6), pp.066105.
22. Wood, C. D. (2006). On-chip THz Systems. PhD thesis, University of Leeds.
23. Yanagi, S., Onuma, M., Kitagawa, J. and Kadoya, Y., 2008. Propagation of terahertz pulses on coplanar strip-lines on low permittivity substrates and a spectroscopy application. *Applied physics express*, 1(1), pp.012009.

24. Kitagawa, J., Kadoya, Y., Suekuni, K., Avila, M.A. and Takabatake, T., 2013. Characterization of terahertz absorption in clathrate compound by compact spectroscopic chip. *Japanese journal of applied physics*, 52(2R), pp.028003.
25. Kasai, S., Tanabashi, A., Kajiki, K., Itsuji, T., Kurosaka, R., Yoneyama, H., Yamashita, M., Ito, H. and Ouchi, T., 2009. Micro strip line-based on-chip terahertz integrated devices for high sensitivity biosensors. *Applied Physics Express*, 2(6), pp.062401.
26. Wu, J., Sydoruk, O., Mayorov, A.S., Wood, C.D., Mistry, D., Li, L., Linfield, E.H., Giles Davies, A. and Cunningham, J.E., 2016. Time-domain measurement of terahertz frequency magnetoplasmon resonances in a two-dimensional electron system by the direct injection of picosecond pulsed currents. *Applied Physics Letters*, 108(9), pp.091109.
27. Qiu, Y., Meng, K., Wang, W., Chen, J., Cunningham, J., Robertson, I., Hong, B. and Wang, G.P., 2023. Efficient free-space to on-chip coupling of THz-bandwidth pulses for biomolecule fingerprint sensing. *Optics Express*, 31(2), pp.2373-2385.
28. Brown, E.R., Bjarnason, J.E., Fedor, A.M. and Korter, T.M., 2007. On the strong and narrow absorption signature in lactose at 0.53 THz. *Applied Physics Letters*, 90(6), pp. 061908.
29. Datta, S., Prasertsuk, K., Khammata, N., Rattanawan, P., Chia, J.Y., Jintamethasawat, R., Chulapakorn, T. and Limpanuparb, T., 2022. Terahertz Spectroscopic Analysis of Lactose in Infant Formula: Implications for Detection and Quantification. *Molecules*, 27(15), pp.5040.
30. Russell, C., Wood, C.D., Burnett, A.D., et al., 2013. Spectroscopy of polycrystalline materials using thinned-substrate planar Goubau line at cryogenic temperatures. *Lab on a Chip*, 13(20), pp.4065-4070.
31. Amarloo, H. and Safavi-Naeini, S., 2021. Enhanced on-chip terahertz vibrational absorption spectroscopy using evanescent fields in silicon waveguide structures. *Optics Express*, 29(11), pp.17343-17352.

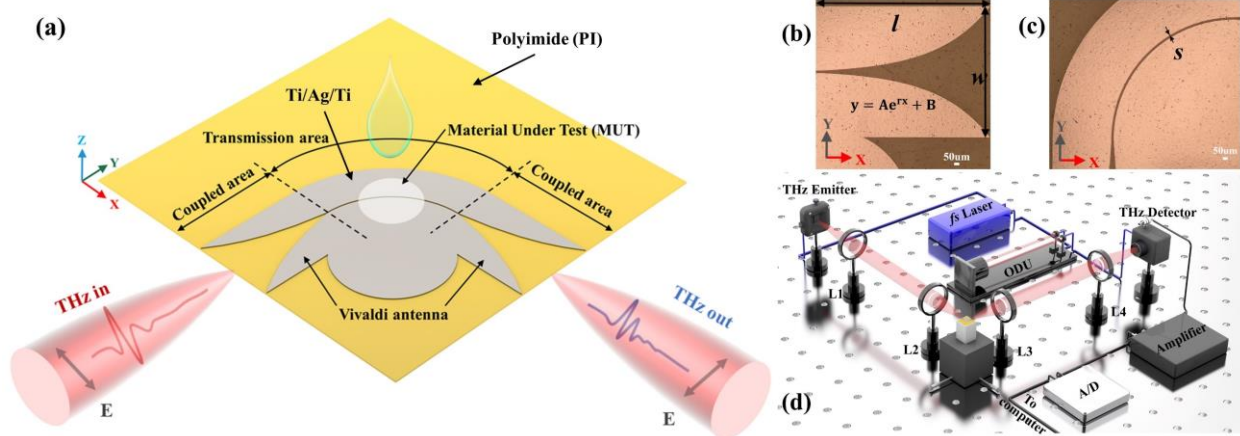


Figure 1: **Schematic of the THz sensing chip and experimental set-up.** (a) THz pulses are coupled to and from the chip via Vivaldi antennas. The slotline waveguide features a 90° bend to eliminate line-of-sight signals. (b) and (c) Micrographs of on-chip waveguides, with dimensions $w=0.62$ mm, $l=1.6$ mm, and $s=25$ μm. The Vivaldi antenna edges follow the exponential function $y=Ae^{rx}+B$, where A, B, and r are constants (d) Experimental setup for measuring the 90° bent THz sensing chip. Blue and black lines represent optical fibers and electronic cables; the red area shows the THz optical path. L1 - L4 are TPX lenses. fs: femtosecond. ODU: optical delay unit. A/D: analog-to-digital converter.

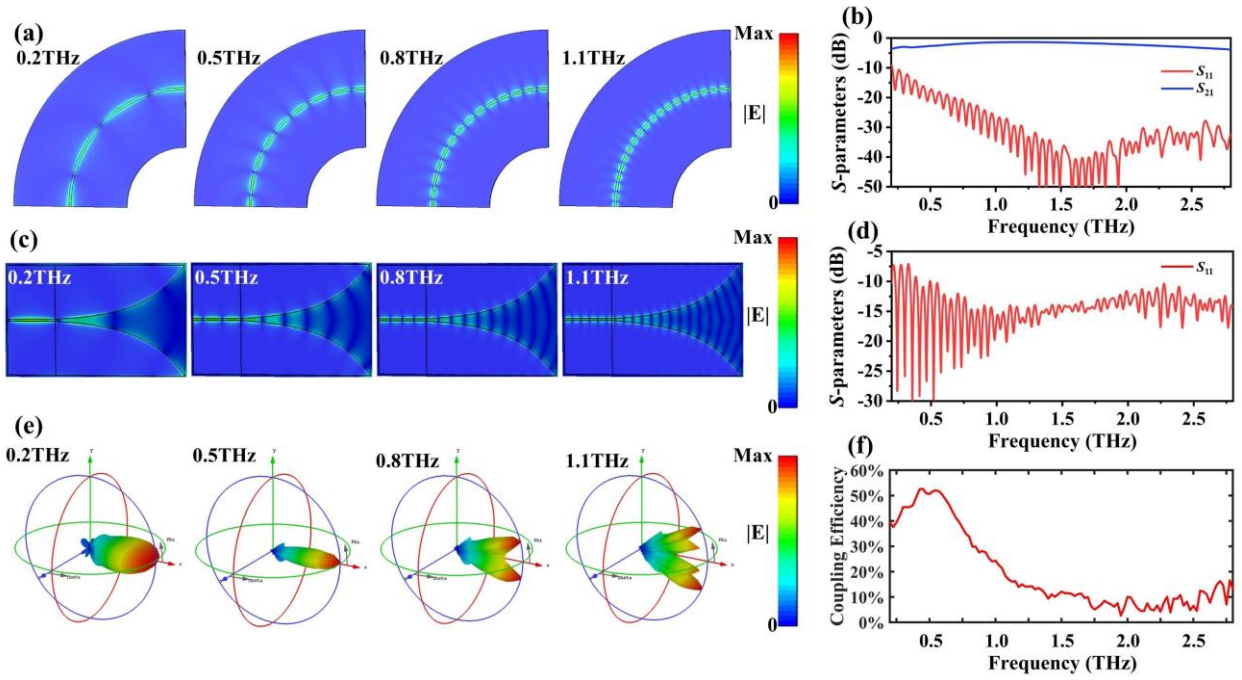


Figure 2: **Simulation results for the slotline waveguide and Vivaldi antenna.** (a) Normalized electric field $|E|$ propagating along the slotline waveguide. (b) Simulated S-parameters for the 90° bent slotline waveguide. (c) Near-field wave propagation pattern of the Vivaldi antenna. (d) Reflection coefficients of the Vivaldi Antenna. (e) 3D far-field radiation pattern of the Vivaldi antenna. (f) Coupling Efficiency of the Vivaldi antenna calculated by using both measured and simulated data

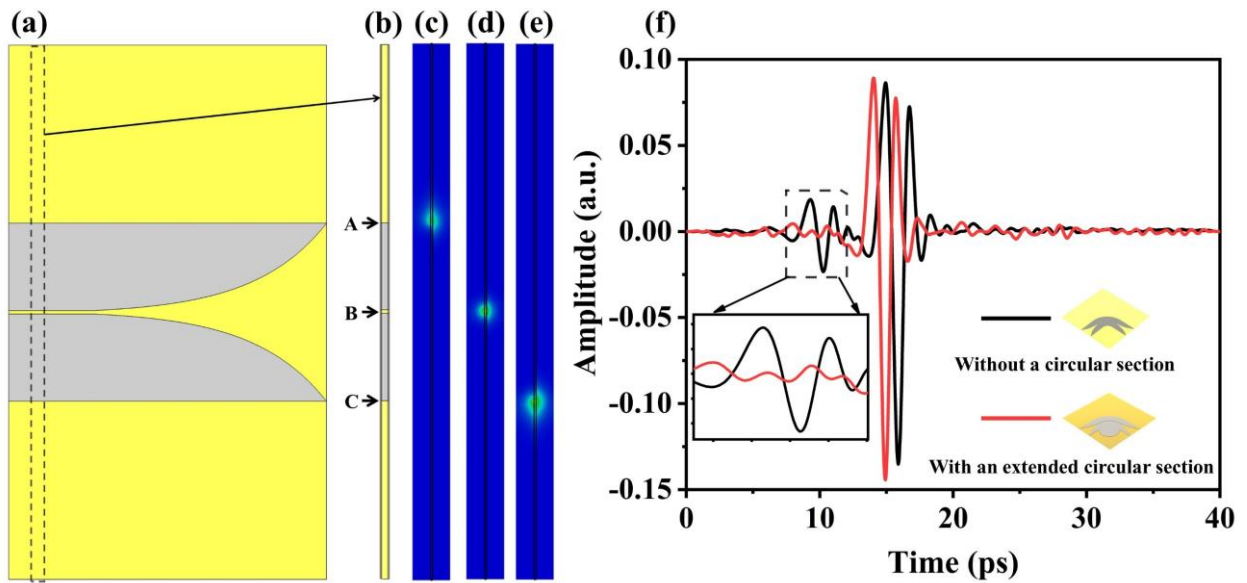


Figure 3: **Eigenmode analysis and measured time-domain signals of the unloaded sensing chip.** (a) Schematic of the conjoint slotline waveguide and Vivaldi Antenna. (b) Unit cell of the slotline waveguide (length: $25\ \mu\text{m}$) used in CST. (c)-(e) Electric field diagrams at the 90° bend in the slotline waveguide from CST (logarithmic scale): (c) unwanted competing mode 1 (CM1), (d) desired fundamental mode (FM), (e) unwanted competing mode 2 (CM2). (f) Measured time-domain signal of the unloaded chip with (red) and without (black) an extended circular section in the waveguide. Inset: Oscillation before the primary pulse at 15 ps.

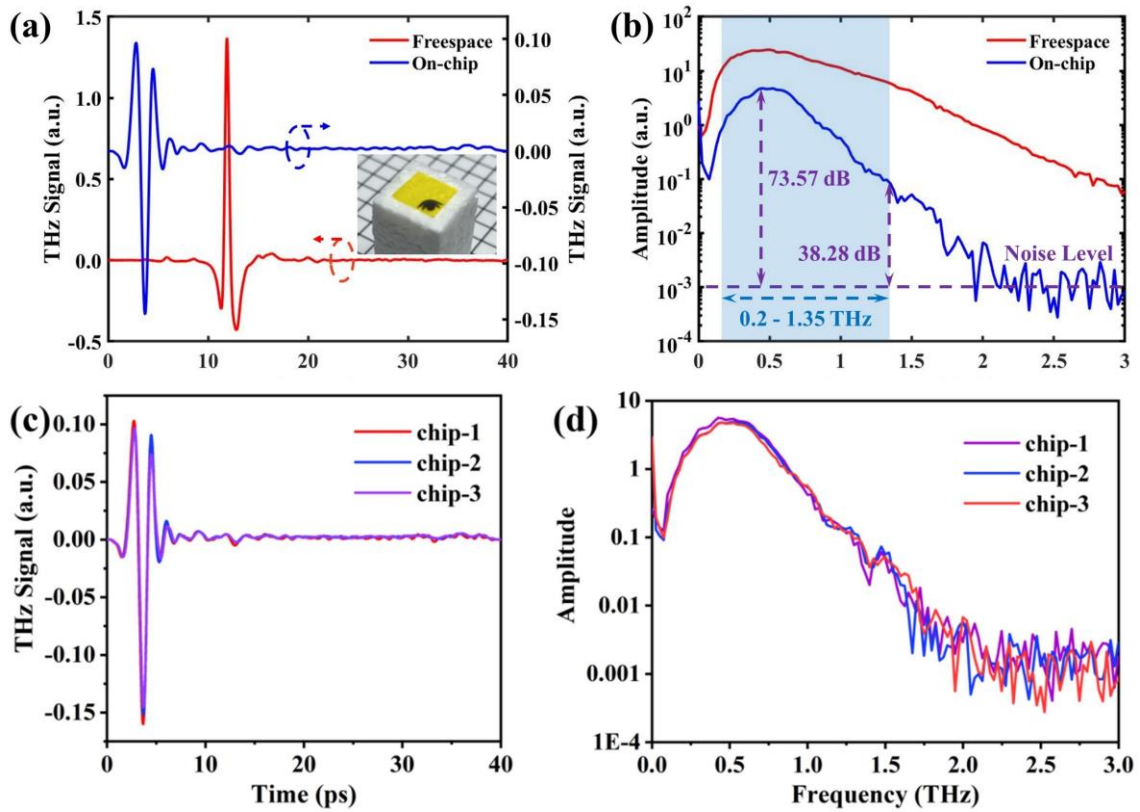


Figure 4: **THz signals and spectrum of sensing chip.** (a) Measured THz time-domain signal with and without the sensing chip; inset shows the chip on EPS foam. (b) Frequency spectra corresponding to the signal in (a). (c) Measured THz signals of various sensing chips. (d) Frequency spectrum of the signals in (c).

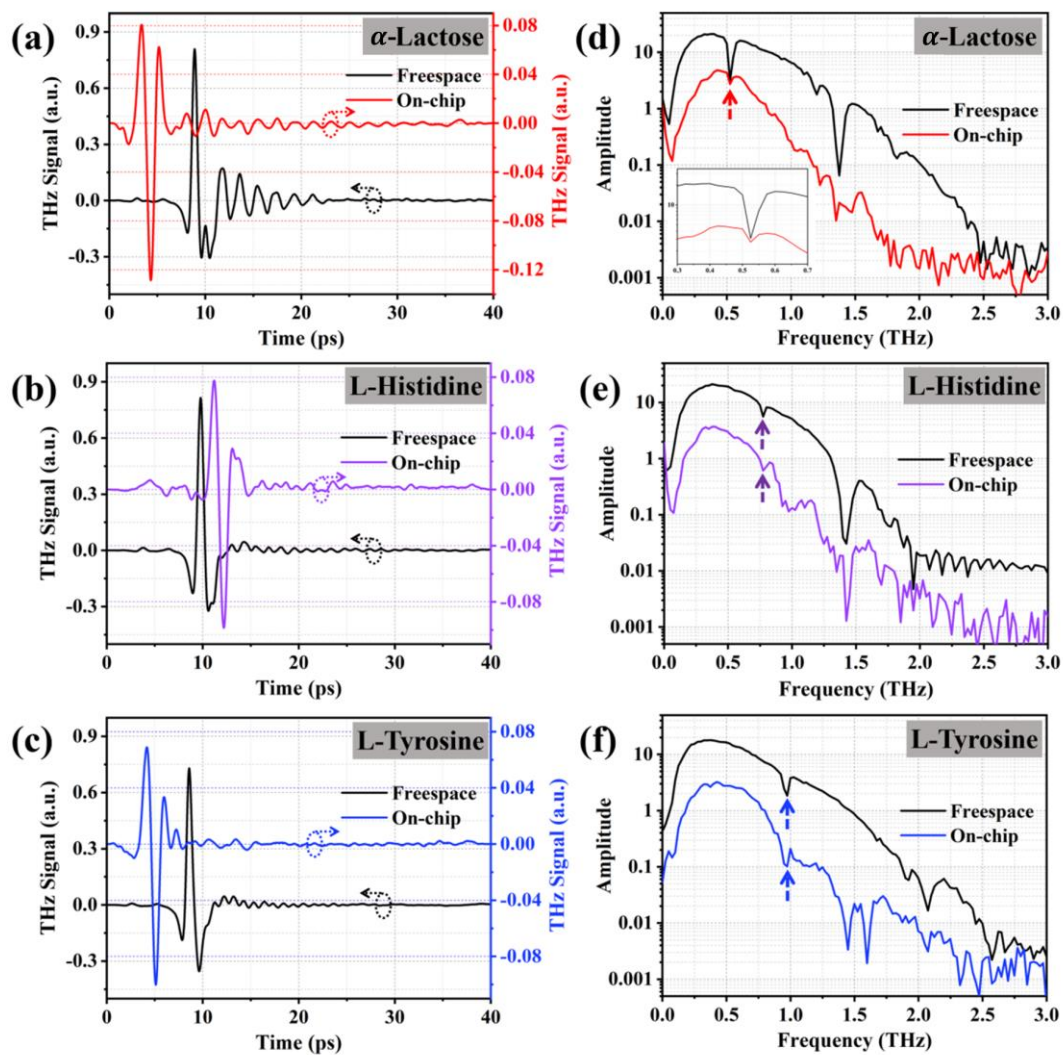


Figure 5: **THz signals and spectra of three powders measured by the sensing chip and in free space.** The color curve represents the chip measurements, while the black curve indicates free space measurements. (a)-(c) THz signals of α -lactose monohydrate, L-histidine, and L-tyrosine, respectively. (d)-(f) Spectra of the three powders, respectively.

Table 1. The free-space and on-chip absorption fingerprints of various different biomolecular powders.

	Method*	Absorption Fingerprints	Mass
α -lactose monohydrate	Free-space	0.525 THz	~10 g
	On-Chip	0.525 THz	1.0 mg
L-histidine	Free-space	0.774 THz	~10 g
	On-Chip	0.774 THz	1.1 mg
L-tyrosine	Free-space	0.974 THz	~10 g
	On-Chip	0.974 THz	0.3 mg

* The free-space method uses a large powder sample wrapped in PP film, while the on-chip method transfers a small amount to the slotline waveguide gap with a powder spoon.

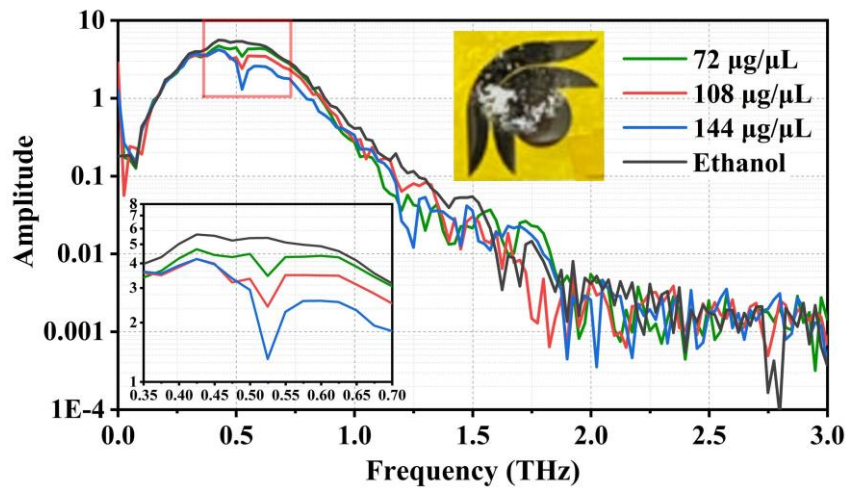


Figure 6: **The detected absorption fingerprints of α -lactose monohydrate with different concentrations.** The volume of the ethanol used in the lactose-ethanol suspension is 0.8 μL . The net weights of the α -lactose monohydrate powder after evaporation of the ethanol solvent are 57.6 μg , 86.4 μg , and 115.2 μg , corresponding to 72 $\mu\text{g}/\mu\text{L}$, 108 $\mu\text{g}/\mu\text{L}$, and 144 $\mu\text{g}/\mu\text{L}$, respectively.

Table 2. Comparison of Broadband THz Spectroscopy Studies on α -Lactose Monohydrate

ID	Method	Operating Frequency	Absorption Peaks	Lactose Concentration	Lactose Treatment	Year	Study
1	Free-space THz-TDS	0.1 – 3 THz	0.58 THz	Not specified	Tablet (powder compression)	2004	[7]
2		0.3 – 1.6 THz	0.5 THz	Not specified	Pellet (powder compression)	2007	[28]
3		0 – 2 THz	0.53 THz	10 mg	Pellet (powder compression)	2022	[29]
4	On-chip THz-TDS	0.1 – 0.8 THz	0.534 THz	Not specified	Pellet (powder compression)	2008	[18]
5		0 – 2 THz	0.531 THz	40 mg	Pellet (powder compression)	2013	[30]
6		0.5 – 0.58 THz	0.532 THz	20 mg	Powder	2021	[31]
7		0.2 – 1.15 THz	0.53 THz	1 mg	Powder	2023	[27]
8		0.2 – 1.35 THz	0.525 THz	57.6 μ g (72 μ g/ μ L)	Powder (solution titration)	2024	This work